JCB Journal of Cell Biology

REPORT

Reticulons promote formation of ER-derived double-membrane vesicles that facilitate SARS-CoV-2 replication

Jeffrey M. Williams[1*], Yu-Jie Chen[1*], Woo Jung Cho[2], Andrew W. Tai[3], and Billy Tsai[1]

Severe acute respiratory syndrome coronavirus-2 (SARS-CoV-2), the etiologic agent for the global COVID-19 pandemic, triggers the formation of endoplasmic reticulum (ER)-derived replication organelles, including double-membrane vesicles (DMVs), in the host cell to support viral replication. Here, we clarify how SARS-CoV-2 hijacks host factors to construct the DMVs. We show that the ER morphogenic proteins reticulon-3 (RTN3) and RTN4 help drive DMV formation, enabling viral replication, which leads to productive infection. Different SARS-CoV-2 variants, including the delta variant, use the RTN-dependent pathway to promote infection. Mechanistically, our results reveal that the membrane-embedded reticulon homology domain (RHD) of the RTNs is sufficient to functionally support viral replication and physically engage NSP3 and NSP4, two viral non-structural membrane proteins known to induce DMV formation. Our findings thus identify the ER morphogenic RTN3 and RTN4 membrane proteins as host factors that help promote the biogenesis of SARS-CoV-2-induced DMVs, which can act as viral replication platforms.

Introduction

Severe acute respiratory syndrome coronavirus 2 (SARS-CoV-2) is responsible for the global COVID-19 pandemic (Dong et al., 2020; Lu et al., 2020; Zhou et al., 2020; Zhu et al., 2020, Coronaviridae Study Group of the International Committee on Taxonomy of Viruses, 2020). To cause infection, SARS-CoV-2 undergoes endocytosis to reach the endosome where the viral and endosomal membranes fuse, delivering the viral genomic RNA (gRNA) into the cytosol (Hoffmann et al., 2020; Walls et al., 2020). ORF1a and ORF1b of the incoming viral gRNA are translated into two polypeptides, pp1a and pp1ab, via a programmed-1 ribosomal frameshift (Chen et al., 2020a; Pohl et al., 2022; Sawicki et al., 2007). Cotranslational and posttranslational cleavage of pp1a and pp1ab gives rise to 16 non-structural proteins (NSPs). NSP2–16 make up the viral replication and transcription complex (RTC) enabling genome replication by performing various functions including RNA synthesis, proofreading, processing, and innate immune evasion.

Importantly, a subset of the RTC NSPs is necessary for the formation of ER-derived replication organelles (ROs) that function as sites for viral genome replication (Knoops et al., 2008; Oudshoorn et al., 2017; Snijder et al., 2020; Speckhart et al., 2021; Ulasli et al., 2010). The major RO for coronaviruses is the double-membrane vesicles (DMVs), although other membranous structures have also been proposed as sites of genome amplification and translation (Froshauer et al., 1988; Shang et al., 2022; Singh et al., 2020; Snijder et al., 2020). The DMVs support the transcription of viral gRNA and subgenomic RNAs (sgRNAs) via a process called discontinuous transcription, a hallmark of coronaviruses. Further rounds of translation and polyprotein cleavage leading to the formation of more RTCs are iterative processes that result in the amplification of DMVs, replicated viral gRNAs, and sgRNAs. The sgRNAs encode four viral structural proteins S, E, M, and N, along with 11 accessory proteins (Kim et al., 2020; Sawicki and Sawicki, 1995). The gRNAs and different sgRNAs are then exported from inside the DMVs into the cytosol (Wolff et al., 2020b) via a putative pore in the DMV containing NSP3 (Wolff et al., 2020a). Those sgRNAs encoding S, E, and M are targeted to the ER where translation generates the S, E, and M membrane proteins, while the sgRNAs encoding the N protein are translated in the cytosol. The N

[1]Department of Cell and Developmental Biology, University of Michigan Medical School, Ann Arbor, MI, USA; [2]Biomedical Research Core Facilities, University of Michigan Medical School, Ann Arbor, MI, USA; [3]Department of Internal Medicine and Department of Microbiology and Immunology, University of Michigan Medical School, Ann Arbor, MI, USA.

*J.M. Williams and Y-J. Chen contributed equally to this work. Correspondence to Billy Tsai: btsai@umich.edu; Yu-Jie Chen: chenyuj@med.umich.edu.

protein associates with the gRNA, and the resulting complex is targeted to the ER–Golgi intermediate compartment (ERGIC) where it assembles with the S, E, and M proteins. In the final step, the assembled viral particles exit the host cell via a secretory pathway (Chen et al., 2020a; Klaus et al., 2013; Klumperman et al., 1994; McBride et al., 2007; Stertz et al., 2007; V'Kovski et al., 2021).

Despite this level of understanding of the SARS-CoV-2 life cycle, major gaps remain including how the virus induces the formation of the DMVs that support viral replication. For SARS-CoV-2 and the related SARS-CoV, and the Middle East Respiratory Syndrome-related coronavirus (MERS-CoV), the viral non-structural membrane proteins NSP3, NSP4, and NSP6 are crucial for ER membrane remodeling, leading to the formation and maintenance of the DMVs (Angelini et al., 2013; Knoops et al., 2008; Oudshoorn et al., 2017; Snijder et al., 2020; Wolff et al., 2020a; Wolff et al., 2020b). NSP6 was shown to organize DMVs through induced ER membrane "zippering" and to restrict access of the ER luminal machinery to the DMVs (Ricciardi et al., 2022). However, how NSP3, NSP4, and NSP6 act in concert with host factors to generate these viral replication structures is largely unknown.

Here, using infectious SARS-CoV-2, we show that the ER membrane-shaping proteins reticulon-3 (RTN3) and RTN4 are necessary for the efficient formation of DMVs, enabling viral replication, which results in productive infection (Moreira et al., 1999; Schulte and Healy, 1987; van de Velde et al., 1994). The RTNs, including RTN1–4, reside on the outer leaflet of the ER membrane on ER tubules via a conserved reticulon homology domain (RHD; Oertle et al., 2003). The RHD consists of two hydrophobic membrane-embedded hairpins connected by a hydrophilic loop (Di Scala et al., 2005); this domain forms short hairpins that insert into the outer ER leaflet to induce membrane curvature (Shibata et al., 2010; Voeltz et al., 2006). The RHD, located near the C-termini of RTNs, shares ∼70% identity across the RTN family, while the N-termini of the RTNs and their myriad of isoforms lend specificity to each RTN due to alternative splicing (GrandPré et al., 2000). RTN4 is the most well-characterized of the RTNs due to its importance as a neural outgrowth inhibitor in the central nervous system, yet the RTNs are expressed widely across various tissues in mammals (Di Scala et al., 2005; Geisler et al., 1998; Oertle et al., 2003). Our results further demonstrate that multiple SARS-CoV-2 variants, including the delta variant, hijack the RTN-mediated pathway during infection. Structure–function analysis in the context of an overexpression system reveals that the RHD of RTN3 and RTN4—a motif known to induce ER membrane curvature (Chen et al., 2020b; Shibata et al., 2010; Voeltz et al., 2006; Yang and Strittmatter, 2007; Zurek et al., 2011)—is sufficient to promote viral replication. Finally, we found that the RTNs physically bind to NSP3 and NSP4, two viral non-structural proteins that are necessary to induce DMV formation. Together, our data identify RTN3 and RTN4 as host factors that play a critical role during the biogenesis of SARS-CoV-2-induced DMV structures.

Results and discussion

SARS-CoV-2 exploits RTN3 and RTN4 to support infection

Formation of CoV-induced DMVs requires reshaping of the ER membrane. Based on the known role of RTNs in ER membrane curvature, we tested whether RTN3 and RTN4 (key RTN family members), along with FAM134B (which also harbors an RHD but is localized to ER sheets), play any role during SARS-CoV-2 infection using the siRNA knockdown (KD) approach (Mirabelli et al., 2021; Ou et al., 2020; Zhou et al., 2020; Zhu et al., 2020).

To monitor infection, we incubated human Huh7 cells with the SARS-CoV-2 USA-WA1/2020 variant for 48 h and used the 50% tissue culture infective dose ($TCID_{50}$) assay to measure infectious virus titer secreted from the cells (see Fig. S1 A for a schematic of assays). Importantly, when these RHD-containing proteins are individually knocked down using specific siRNAs for 48 h (Fig. 1 A), depletion of either full-length RTN3 (RTN3A) or full-length RTN4 (RTN4A) and its shorter isoform RTN4B (harboring a slightly truncated cytosolic region), but not FAM134B, reduced virus infection when compared with control (scrambled siRNA-treated) cells (Fig. 1 B; see also Fig. S1 B). We note that although the RTN3 siRNA also reduced the FAM134B level as previously reported (Cunningham et al., 2019), the block in SARS-CoV-2 infection using this siRNA is unlikely due to a lowered FAM134B level because virus infection was unaffected by the FAM134B siRNA, which reduced the FAM134B (but not RTN3A) level. Using a similar approach, we depleted RTN3C (a naturally occurring shorter isoform of RTN3A, see below) and RTN4A/RTN4B in the simian Vero E6 cells (Fig. S1 C); only RTN3C, but not RTN3A, was detected in the Vero E6 cells, similar to simian CV-1 cells as we previously reported (Chen et al., 2020b). These cells were subsequently infected with the SARS-CoV-2 USA-WA1/2020 variant for 48 h followed by the $TCID_{50}$ assay. Importantly, viral infection in these cells was markedly reduced under RTN3 or RTN4 KD (Fig. 1 C; see also Fig. S1 B). RTN3 KD in Huh7 cells also impaired infection by the alpha (B.1.1.7), beta (B1.351), and delta (B1.617.2) SARS-CoV-2 variants (Fig. 1 D; see also Fig. S1 B). As a control, we used the MTS cell viability assay to examine cellular integrity and found that neither depletion of RTN3 nor RTN4 compromised cellular viability at either 48 h or 96 h posttransfection of the siRNAs relative to control cells (Fig. S1 D). Furthermore, using the PCR-based XBP1 splicing assay (Yoshida et al., 2001), no ER stress induction was observed under the KD conditions (Fig. S1 E), consistent with our previous report (Chen et al., 2020b). Moreover, by confocal imaging, we observed that depletion of RTN3 or RTN4 did not dramatically alter global ER morphology (Fig. S1 F). Together, these results demonstrate that RTN3 and RTN4 support SARS-CoV-2 infection across different viral variants.

RTN3 and RTN4 are required for efficient SARS-CoV-2 genome replication

The finding that RTN3 and RTN4 play a functional role in SARS-CoV-2 infection prompted us to ask if replication of the viral genome might be disrupted when these RTN proteins are depleted. Replication of the SARS-CoV-2 genome is thought to occur in the virus-induced DMV (Klein et al., 2020; Snijder et al., 2020). In this replication organelle, dsRNA intermediates are formed during genome replication. Indeed, dsRNA intermediate formation is a hallmark of active CoV replication. To determine if RTN3 and RTN4 play a role in the formation of the dsRNA

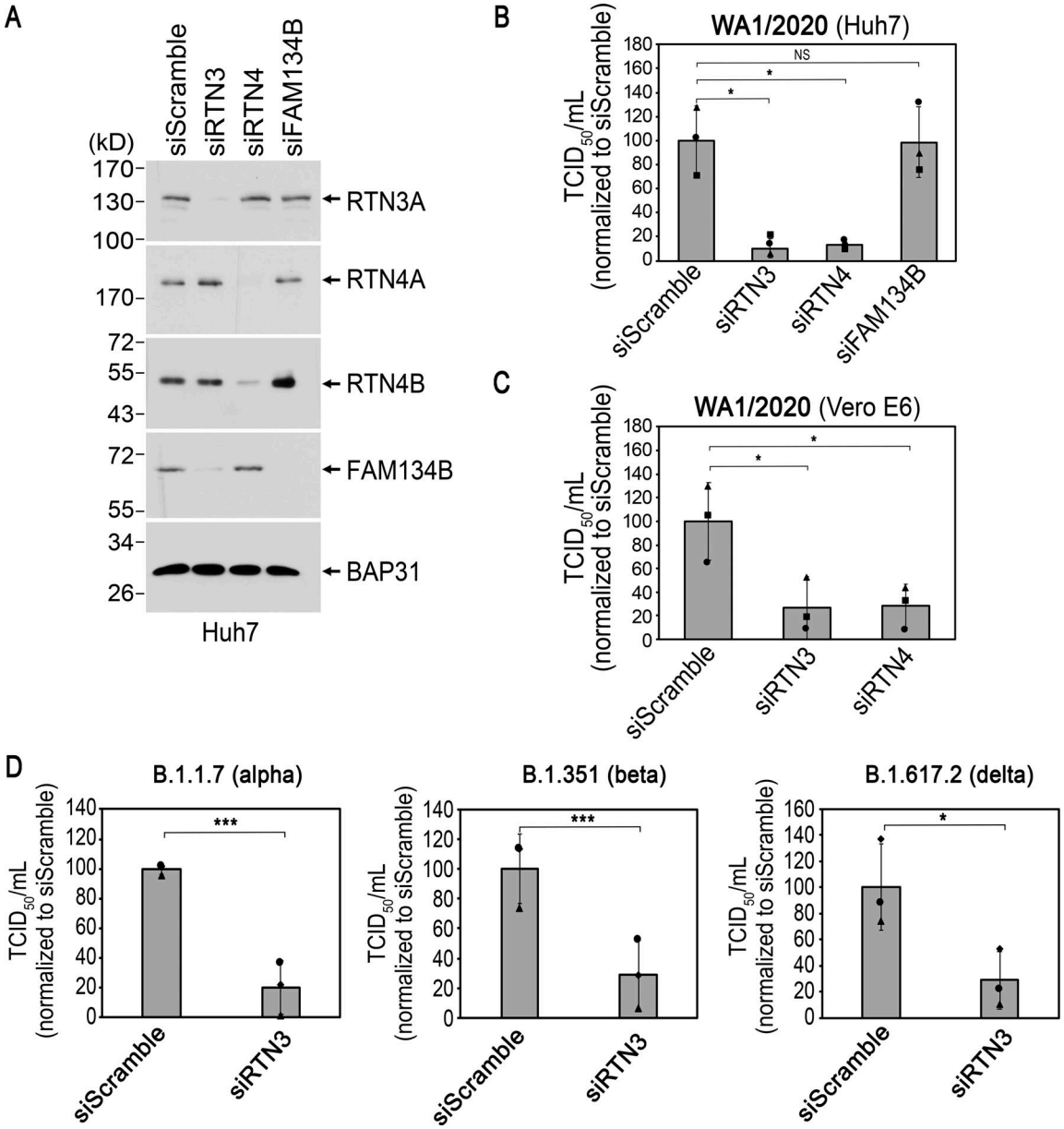

Figure 1. **SARS-CoV-2 exploits RTN3 and RTN4 to support SARS-CoV-2 infection. (A)** siRNA KD of RTN3, RTN4, or FAM134B. Cell extracts derived from Huh7 cells transfected with the indicated siRNA were subjected to SDS-PAGE and immunoblotting with the indicated antibodies. **(B)** Huh7 cells transfected with the indicated siRNAs were infected with SARS-CoV-2 WA1. 48 h after infection, Huh7 media containing the secreted virus was serially diluted onto a 96-well plate of Vero E6 cells. After 48 h, each well was scored for the cytopathic effect (CPE), and the $TCID_{50}$/ml was determined. The graph represents $TCID_{50}$/ml relative to control (scrambled siRNA-treated) cells. Error bars represent means ± SD from three biological replicates. **(C)** Vero E6 cells transfected with the indicated siRNAs were infected with SARS-CoV-2 WA1 for 48 h, and the $TCID_{50}$/ml was determined as in B. Error bars represent means ± SD from three biological replicates. **(D)** Huh7 cells were transfected with the scrambled or RTN3 siRNA and infected with SARS-CoV-2 alpha (B.1.1.7, left panel), beta (B1.351, center panel), and delta (B1.617.2, right panel) variants and the $TCID_{50}$/ml was determined as in B. Graphs represent the $TCID_{50}$/ml relative to control (scrambled siRNA-treated) cells. Error bars represent means ± SD from three biological replicates per variant. **(B–D)** Huh7 cells were infected at 2 MOI with the indicated variants. Results were analyzed using Student's two-tailed *t* test. Data are represented as the mean values, where indicated. The P values are indicated by *P < 0.05, ***P < 0.001. Source data are available for this figure: SourceData F1.

intermediate, Huh7 cells were transfected with the indicated siRNAs for 48 h and subsequently infected with the virus for 48 h and stained with an antibody that selectively detects dsRNA. Our results revealed that RTN3 or RTN4 (but not FAM134B) KD robustly decreased dsRNA formation (Fig. 2 A; quantified in Fig. 2 B). Similarly, depletion of RTN3 or RTN4 in Vero E6 cells also decreased the formation of dsRNA (Fig. 2 C; quantified in Fig. 2 D). We then used quantitative RT-PCR (qRT-PCR) to assess the replicated gRNA level in Huh7 cells infected with the virus for 48 h and found that the gRNA level markedly decreased under RTN3 or RTN4 KD (Fig. 2 E), consistent with the dsRNA staining findings (Fig. 2, A–D). Taken together, these findings indicate that the RTN host proteins play a crucial role during SARS-CoV-2 genome replication. We then examined if

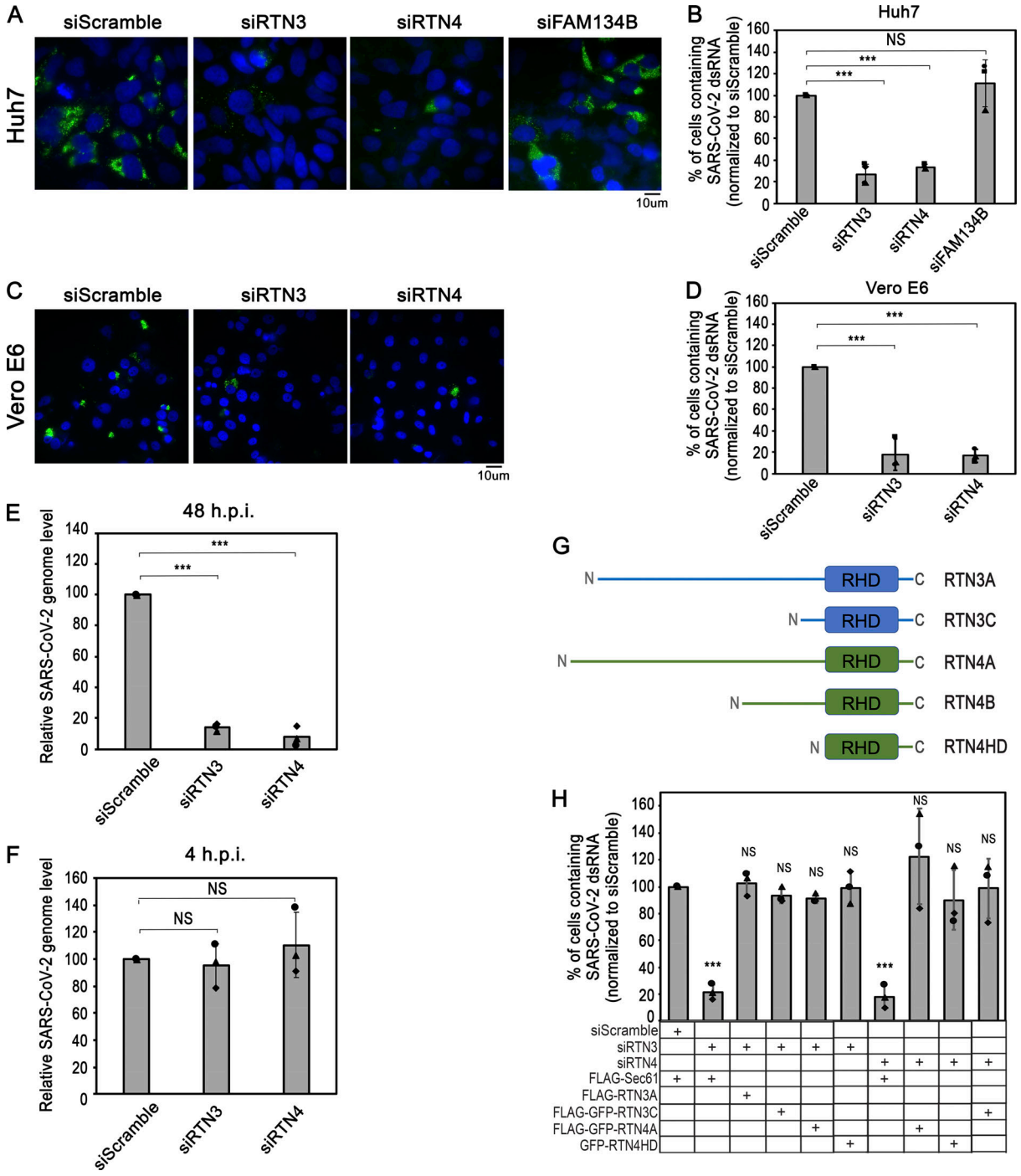

Figure 2. **RTN3 and RTN4 are required for efficient SARS-CoV-2 genome replication. (A)** Huh7 cells were transfected with the indicated siRNAs, infected with SARS-Cov-2 WA1 (2 MOI) for 48 h, and then processed for epifluorescence microscopy. Anti-dsRNA (j2) was stained in green and DAPI in blue. Scale bars, 10 µm. **(B)** Quantification of the percentage of cells positive for dsRNA relative to control (scrambled siRNA-treated) cells for Huh7 cells in A. >100 cells were counted for each condition. Error bars represent means ± SD from three biological replicates. **(C)** Vero E6 cells were transfected with the indicated siRNAs, infected with SARS-CoV-2 WA1 for 48 h at (2 MOI), and then processed for epifluorescence microscopy. Anti-dsRNA (j2) was stained in green and DAPI in blue. Scale bars, 10 µm. **(D)** Quantification of the percentage of cells positive for dsRNA relative to control (scrambled siRNA-treated) cells for Vero E6 cells in C. >100 cells were counted for each condition. Error bars represent means ± SD from three biological replicates. **(E)** Huh7 cells were transfected with the indicated siRNAs, infected with SARS-CoV-2 WA1 for 48 h at 2 MOI, and the total RNA was isolated. RT-qPCR was subsequently performed using primers against Orf1a of SARS-CoV-2. Graph represents relative viral genome levels compared to control (scrambled siRNA-treated) cells. Error bars represent means ± SD from three biological replicates. **(F)** Huh7 cells were transfected with the indicated siRNAs, infected with SARS-CoV-2 WA1 for 4 h at 5 MOI, and the total RNA was isolated. RT-qPCR was subsequently performed as in E. Graph represents relative viral genome levels compared to control (scrambled siRNA-treated) cells. Error bars represent means ± SD from three biological replicates. **(G)** Schematic of the indicated RTN isoforms used to rescue the RTN3 or RTN4 KD cells. **(H)** Huh7 cells were transfected with the indicated siRNAs for 24 h and then transfected with the indicated DNA constructs for 24 h. Cells were then infected and processed as in A and quantified as in B. Error bars represent means ± SD from three biological replicates. Results were analyzed using Student's two-tailed *t* test. Data are represented as the mean values where indicated. The P values are indicated by ***P < 0.001. NS, not significant where only P < 0.05 was considered to be significant.

early events of SARS-CoV-2 infection were affected under RTN3 or RTN4 KD by assessing the level of the viral gRNA (by qRT-PCR) at 4 hpi. At this time point, we found that the viral gRNA level was unaffected by the depletion of RTN3 or RTN4 (Fig. 2 F), suggesting that early events supporting virus genome replication do not require RTN3 and RTN4 (see below).

What structural features of RTN3 and RTN4 assist in SARS-CoV-2 replication? In addition to the RHD that inserts into the ER membrane, RTN3 contains a cytosolic N-terminal domain (NTD) harboring many LC3-interacting regions (LIRs), which participate in an ER-dependent protein quality control process called ER-coupled autophagy (ER-phagy; Chen et al., 2021; Cunningham et al., 2019; Grumati et al., 2017). While full-length RTN3A contains both the RHD and NTD, RTN3C contains only the RHD (Fig. 2 G). In the case of RTN4, full-length RTN4A contains its own cytosolic N-terminal extension followed by the RHD, while an engineered truncated mutant of RTN4 (RTN4HD) contains only its RHD (Fig. 2 G).

Importantly, using a KD-rescue approach, we found that the block in dsRNA formation in RTN3 KD cells can be fully restored by overexpressing either (FLAG- and/or GFP-tagged) RTN3A, RTN3C, RTN4A, or RTN4HD (Fig. 2 H). These findings not only demonstrate that the impaired dsRNA formation observed with RTN3 KD is due to loss of RTN3 (and not to unintended off-target effects) but they also indicate that the RHD domain of RTN3 or RTN4 is sufficient to support SARS-CoV-2 replication. Using a similar approach, we also found that the block in dsRNA formation in RTN4 KD cells can be rescued by overexpressing RTN4A, RTN4HD, or importantly, RTN3C (Fig. 2 H). The observation that overexpressing RTN4HD can rescue the defect in RTN3 KD cells (and vice versa, overexpressing RTN3C can rescue the impairment in RTN4 KD cells) clearly indicates that the presence of the RHD is an important feature in supporting viral replication.

RTN3 and RTN4 are necessary for DMV formation

Our data thus far suggest that RTN3 and RTN4 support virus replication. As these RTN proteins function to shape the ER membrane, a process that likely plays a key role in DMV formation, we asked if DMV formation itself requires RTN3 or RTN4. To test this, we infected control, RTN3, and RTN4 KD cells with WA1 SARS-CoV-2 for 12 h (or 24 h) and subjected the samples to transmission electron microscopy (TEM). In control cells (infected for 12 h), clusters of double membrane structures proximal to the nucleus and measuring ∼200–300 nm in diameter were readily identified (Fig. 3 A). These physical features are in complete agreement with previously published SARS-CoV-2-induced DMV structures (Klein et al., 2020); additional examples of the virus-induced DMVs are found in Fig. S2 A. Quantification revealed that 17 of the 53 infected cells (32%) that were evaluated contained the DMV clusters (Fig. 3 D). Kinetic analysis found that these DMV structures were not observed at 8 hpi and rarely observed at 10 hpi (<1%) in the control cells (data not shown). By contrast, when 34 RTN3 KD cells (infected for 12 h) were analyzed, none of them displayed the perinuclear DMV clusters (Fig. 3 B, left; quantified in Fig. 3 D; see Fig. S2 B for additional examples). Moreover, only one of the 39 RTN3 KD cells (2.6%) infected for 24 h harbored the DMV clusters (Fig. 3 B, right; quantified in Fig. 3 D). When RTN4 KD cells were evaluated, none of them contained the DMV clusters regardless of the time points (Fig. 3 C; quantified in Fig. 3 D; see Fig. S2 C for additional examples). By TEM, the general ER morphology in the control and RTN-depleted cells were largely indistinguishable (Fig. S3, where the ER is highlighted in red), consistent with the confocal imaging data (Fig. S1 E). This suggests that the level of depletion of the RTN proteins resulting from siRNA-mediated KD does not globally alter the ER morphology in these cells.

Intriguingly, although the DMV structures at 12 hpi were absent under RTN3 or RTN4 KD, the levels of NSP3 (critical for DMV formation) and NSP1 were not affected under the KD conditions at this same time point in the Huh7 cells (Fig. S4 A; quantified in Fig. S4 B); a similar result was found in the Vero E6 cells (Fig. S4 C). As the NSPs observed at 12 hpi likely result from the translation of the replicated virus genome, these findings indicate that at least some degree of genome amplification and translation during early events of SARS-CoV-2 infection (i.e., up to 12 hpi) must occur outside of the RTN3/4-dependent DMVs (see Discussion), as suggested by findings in Fig. 2 F.

RTN3 and RTN4 bind to NSP3 and NSP4

As the ectopic expression of the CoV non-structural proteins NSP3 and NSP4 can induce the formation of DMVs (Angelini et al., 2013), we asked whether these two viral proteins might bind to RTN3 and RTN4. Cells expressing FLAG-tagged RTN3A (FLAG-RTN3A), FLAG and GFP-tagged RTN3C (FLAG-GFP-RTN3C), or the control ER membrane protein Hrd1 (FLAG-Hrd1) were cotransfected with Strep-tagged NSP3 (2xStrep-NSP3) and NSP4 (NSP4-2xStrep), or with either 2xStrep-NSP3 or NSP4-2xStrep alone. In cells expressing 2xStrep-NSP3 and NSP4-2xStrep, we found that immunoprecipitation of either FLAG-RTN3A or FLAG-GFP-RTN3C (but not FLAG-Hrd1) pulled down both 2xStrep-NSP3 and NSP4-2xStrep (Fig. 4 A, top panel, compare lanes 2 and 3 to 1). These findings indicated that RTN3 can bind to NSP3 and NSP4, and suggest that this interaction is mediated by the RHD of RTN3. These results are consistent with the observation that RTN3C (harboring only the RHD) is sufficient to promote dsRNA formation (Fig. 2 H). We also found that in cells expressing FLAG-RTN3A and cotransfected with either 2xStrep-NSP3 or NSP4-2xStrep, precipitation of FLAG-RTN3A can pull down NSP3 and NSP4 (Fig. 4 A, top panel, lanes 4 and 5), demonstrating that RTN3 can individually engage the non-structural proteins.

To study the interaction between RTN4 and NSP3/4, cells expressing 2xStrep-NSP3, NSP4-2xStrep, and another viral non-structural protein FLAG-NSP2, which is not involved in DMV formation, were co-transfected with either the control HA-GFP or HA-RTN4B; as indicated, RTN4B bears a shorter cytosolic domain than RTN4A (Fig. 2 G). We found 2xStrep-NSP3 and NSP4-2xStrep (but not FLAG-NSP2) coprecipitated with HA-RTN4B but not HA-GFP (Fig. 4 B), indicating that RTN4 binds to NSP3 and NSP4; the observation that NSP2 does not bind to RTN4 suggests that the RTN3/4-NSP3/4 interaction is specific. As NSP3 and NSP4 are sufficient to trigger coronavirus DMV biogenesis (Angelini et al., 2013), our physical interaction data further links RTN3 and RTN4 to the DMV formation process.

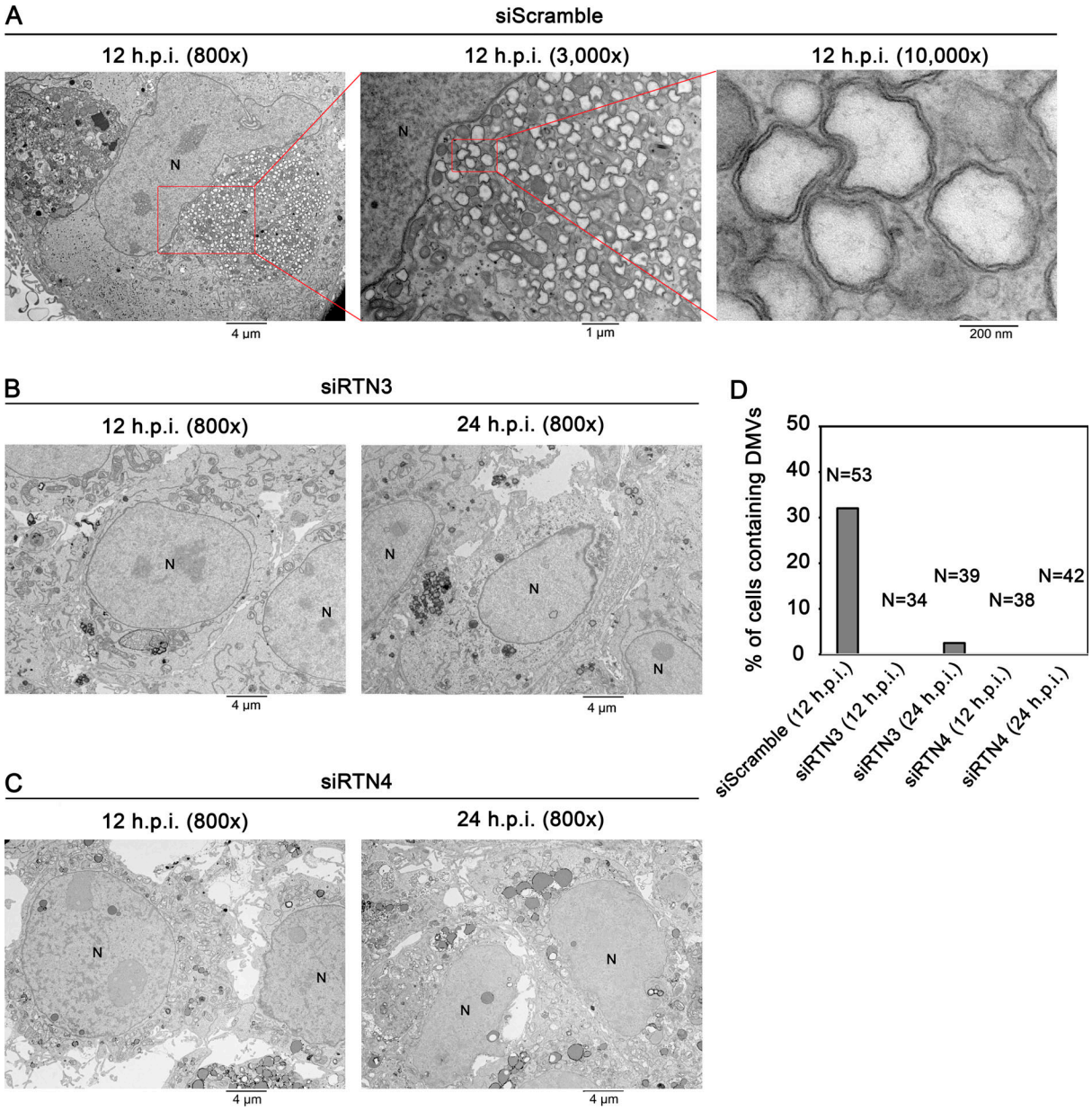

Figure 3. **RTN3 and RTN4 are necessary for DMV formation. (A–C)** Huh7 cells were transfected with the indicated siRNAs and infected with SARS-CoV-2 WA1 for either 12 h or 24 h at 2 MOI. Cells were fixed with glutaraldehyde and processed for conventional TEM. Representative images are shown for each condition where the magnification level is indicated above each image. N denotes the nucleus. **(A)** Representative TEM images showing a peri-nuclear patch of SARS-CoV-2-induced DMVs (left and center). The magnification was increased to clearly reveal the double membrane structures (right). Scale bars (left to right), 4 µm, 1 µm, 200 nm. **(B and C)** Representative TEM images from cells depleted of RTN3 (B) or RTN4 (C). Scale bars, 4 µm. **(D)** Quantification indicating the percentage of cells containing DMVs relative to total cells counted for each condition. N indicates the number of cells counted for that condition.

Coimmunoprecipitation between the RTN proteins and NSP3/NSP4 does not necessarily indicate that these interactions are direct. To evaluate if the RTN-NSP interaction is direct, we isolated FLAG-RTN3A, FLAG-GFP-RTN4A, 2xStrep-NSP3, NSP4-2xStrep, and the control FLAG-GFP from transfected HEK293T cells (Fig. 4 C). We then performed in vitro pull-down studies using these highly-enriched proteins. When 2xStrep-NSP3 was incubated with FLAG-GFP, FLAG-RTN3A, or FLAG-GFP-RTN4A, precipitation of 2xStrep-NSP3 pulled down only the RTN proteins and not GFP (Fig. 4 D, lanes 1–3). Similarly, when NSP4-2xStrep was incubated with FLAG-GFP, FLAG-RTN3A, or FLAG-GFP-RTN4A, precipitation of NSP4-2xStrep pulled down RTN3A, RTN4A, but not GFP (Fig. 4 D, lanes 4–6). These findings strongly suggest that the RTN–NSP interaction is direct.

In this manuscript, we identified RTN3 and RTN4 as ER membrane proteins that promote the formation of ER-derived DMV structures, which facilitate SARS-CoV-2 replication (Fig. 4 E). As DMV formation almost certainly involves curvature of the ER membrane, it is not surprising that RTN3 and RTN4, morphogenic proteins that remodel the ER membrane, mediate DMV formation. For the flavivirus HCV, which also induces DMVs to

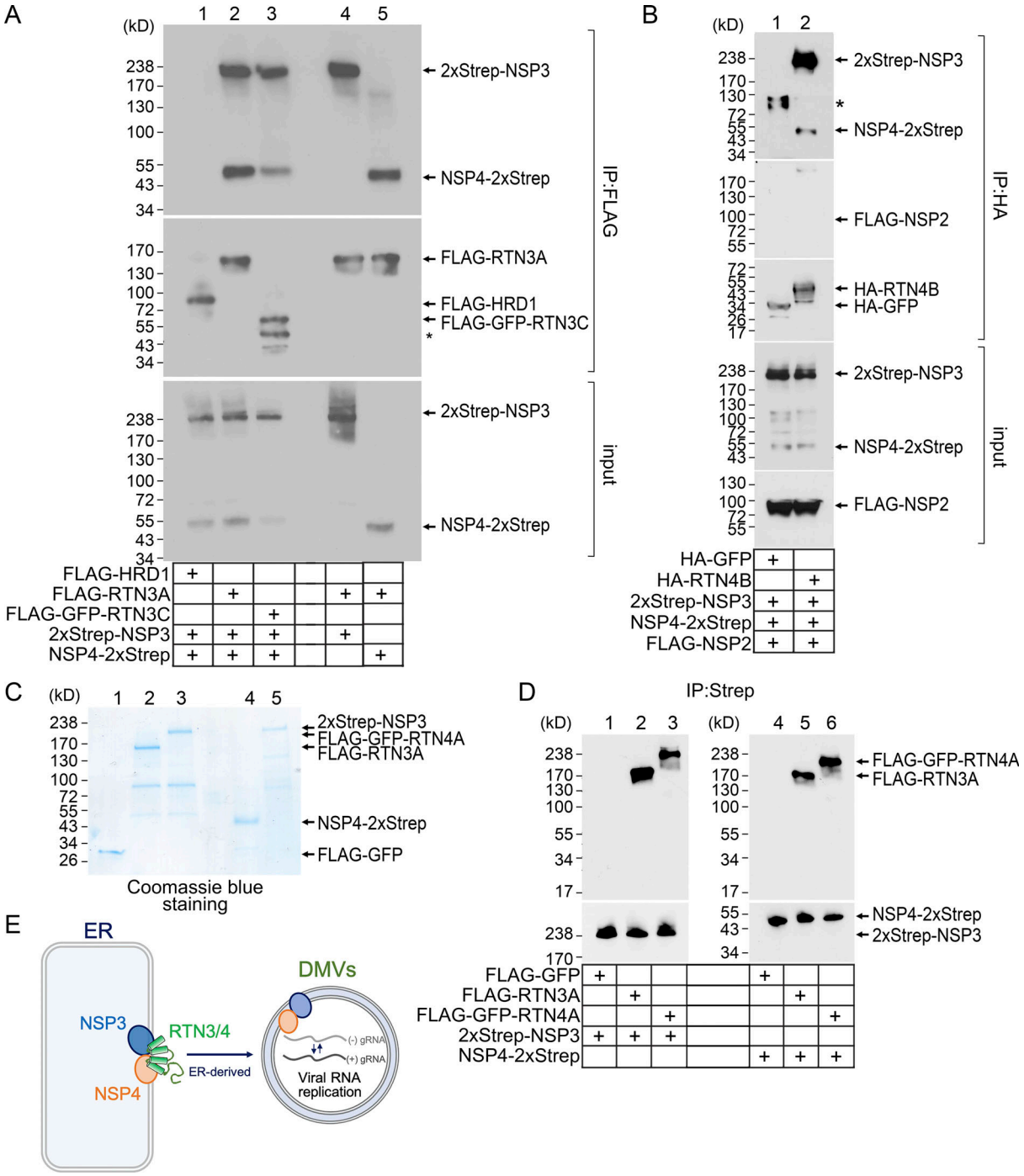

Figure 4. **RTN3 and RTN4 bind to NSP3 and NSP4. (A and B)** HEK 293T cells were transfected with the indicated DNA constructs for 24 h, and the resulting cell extracts were immunoprecipitated (IP) with anti-FLAG (A) or anti-HA (B). The precipitated material was subjected to SDS-PAGE and immunoblotting with the indicated antibodies. Input represents 5% of the total sample used for the IP. * denotes a non-specific unidentified protein. **(C)** FLAG-GFP (lane 1), FLAG-RTN3A (lane 2), FLAG-GFP-RTN4A (lane 3), NSP4-2xStrep (lane 4), and 2xStrep-NSP3 (lane 5) constructs were transfected in HEK293T cells, isolated, and subjected to Coomassie staining. **(D)** Lanes 1–3: 2xStrep-NSP3 was incubated with FLAG-GFP, FLAG-RTN3A, or FLAG-GFP-RTN4A, and the samples subjected to anti-Strep immunoprecipitation. The precipitated material was further subjected to SDS-PAGE followed by immunoblotting with the indicated antibodies. Lanes 4–6: As in lanes 1–3, except NSP4-2xStrep was used instead of 2xStrep-NSP3. **(E)** Schematic summarizing the key finding that the RTN3 and RTN4 ER membrane proteins, which bind to the viral non-structural proteins NSP3 and NSP4, help to promote the formation of the ER-derived DMV structures that participate in SARS-CoV-2 genome replication. Source data are available for this figure: SourceData F4.

support its genome replication (Paul et al., 2013), RTN3 was shown to have both pro- and anti-replicative functions (Diaz and Ahlquist, 2012; Wu et al., 2014). Interestingly, RTN3 was observed in close proximity to SARS-CoV-2 DMVs in the perinuclear region by costaining for dsRNA and RTN3 using confocal microscopy (Cortese et al., 2020). Likewise, using a proximity-labeling approach, RTN4 was found to be proximal to the RTC of the murine coronavirus MHV (V'Kovski et al., 2019). Thus, while evidence indicated that RTNs are proximal to coronavirus RTCs, whether these morphogenic factors play an active role in SARS-COV-2 infection was not entirely clear until now.

Using a siRNA-mediated KD strategy, we found that depletion of RTN3 or RTN4 reduced SARS-CoV-2 infection, dsRNA intermediate formation, replication of the viral genome, and appearance of perinuclear DMV clusters, without impairing early events of viral infection and overall cellular integrity. Along with these loss-of-function data, the physical interaction studies—conducted in an overexpression context—revealed that the RTNs directly engage NSP3 and NSP4, viral non-structural proteins capable of triggering coronavirus DMV formation (Angelini et al., 2013). Although it is unclear if the RTNs are present on the DMVs, our observation that RTNs bind to NSP3 and NSP4 raises this possibility. Together, the functional and biochemical findings strongly suggest that RTN3 and RTN4 help to promote the formation of DMVs during SARS-CoV-2 infection. As DMV formation represents a general process that supports genome replication of the coronavirus family, our identification of two critical host factors required for DMV biogenesis is likely to have a broad impact on our understanding of the infection mechanism of existing (and future) SARS-CoV-2 variants.

Interestingly, our results showed that during early events of virus replication (up to 12 hpi), depletion of the RTN proteins did not affect the NSP levels but decreased the level of the DMVs. If we assume the observed NSPs at this time point are due to translation of the replicated virus genome, these findings raise the possibility that at least some degree of genome amplification and translation during early events of SARS-CoV-2 infection must occur outside of the RTN3/4-dependent DMVs. This possibility is consistent with the idea that genome replication for coronaviruses (and other RNA viruses) can take place in other replication structures, including convoluted membranes, small spherule invaginations, zippered ER compartments, and double membrane spherules, some of which may even be associated with endosomes, lysosomes, and mitochondria (Froshauer et al., 1988; Shang et al., 2022; Singh et al., 2020; Snijder et al., 2020). Moreover, it has also been shown that the number and size of DMVs may not correlate with virus replication (Al-Mulla et al., 2014).

Mechanistically, we then used a KD-rescue approach to identify crucial features in the RTNs that support viral replication and found that the membrane-embedded RHD (consisting of two hairpin loops) is sufficient to support viral replication. As the RHD is inserted into the outer leaflet of the ER membrane, it imposes positive membrane curvature at the site of recruitment. We postulate that this membrane-bending activity shapes the ER membrane leading to DMV formation.

Whether RTN3 and RTN4 execute the exact same function during DMV formation is not entirely clear. However, the observation that RTN4 overexpression can rescue a defect caused by RTN3 KD (and that RTN3 overexpression can restore the impairment due to RTN4 KD) suggests that these two ER membrane proteins may display some degree of overlapping function. If this is true, why are both proteins essential during DMV formation, given that depletion of each individual protein is sufficient to cause a severe phenotype? One possibility is that an overall "threshold" density of the RTNs in the ER membrane is required to efficiently generate DMVs, such that depleting the level of either protein creates a subthreshold condition that prevents the proper formation of these replicative structures. It is important to note that not all RHD-containing proteins promote the formation of SARS-CoV-2 DMVs since depletion of FAM134B (which harbors an RHD) did not block virus infection. One explanation is that other RHD-containing ER proteins are not recruited to the site of developing DMVs and therefore exert little or no effect on DMV formation. This is supported by the observation that FAM134B is enriched in ER sheets to facilitate selective autophagy of this subcellular region, while RTN3 and RTN4 are enriched in ER tubules (Khaminets et al., 2015) to help shape and expand the tubules themselves.

A critical unanswered question is how RTNs coordinate with NSP3 and NSP4 to create DMVs. The exact mechanism of DMV formation from the ER remains unknown and has been proposed to involve membrane budding, tubule elongation, and membrane closure (Klein et al., 2020; Klumperman et al., 1994; Knoops et al., 2008; Miller and Krijnse-Locker, 2008). Thus, it is conceivable that one or more of these membrane remodeling steps require the curvature-inducing activity of RTN3 and RTN4, along with their localization to ER tubules. In one scenario, the NSP3–NSP4 protein complex may bind to and recruit the RTNs to a select region in the ER to initiate DMV formation. Thus, NSP3 and NSP4 simply act as a scaffold to recruit the ER morphogenic factors. Alternatively, given that NSP3 and NSP4 have also been reported to harbor membrane-shaping activities (Hagemeijer et al., 2014; Oudshoorn et al., 2017), the combined actions of the RTNs and these viral non-structural proteins may be necessary to complete the complex reactions leading to DMV formation. This complexity is further underscored by the recent discovery that two ER membrane factors—VMP1 and TMEM41B, which participate in the autophagy process (Ji et al., 2022)—play a role in the biogenesis of coronavirus DMVs. Clearly understanding how the RTNs coordinate with these autophagy factors to help drive DMV formation deserves future investigation.

Materials and methods

Cell lines and reagents

HEK 293T (CRL-3216) and Vero E6 cells (CRL-1586) were obtained from ATCC. The Huh7 cells are from Sekisui Xenotech (JCRB0403)—the US distributor for the Japanese Collection of Research Bioresources (JCRB) Cell Bank—which is supported by the Japanese National Institute of Biomedical

Innovation. All cells were cultured at 37°C under 5% CO_2 in complete DMEM containing 10% FBS or 2% FBS during viral infection, 10 µ/ml penicillin, and 10 µg/ml streptomycin (GIBCO). DMEM, Opti-MEM, and 0.25% trypsin-EDTA were purchased from Thermo Fisher Scientific. FBS was purchased from R&D Systems.

Chemicals and antibodies

Deoxy Big CHAP (DBC), 2-mercaptoethanol (BME), phenylmethylsulphonyl fluoride (PMSF), Triton X-100, and anti-FLAG M2 antibody-conjugated agarose beads (A2220) were purchased from Sigma-Aldrich. 16% w/v paraformaldehyde (PFA), Tween 20, glutaraldehyde (2.5%) in sodium cacodylate buffer, and anti-HA magnetic beads (88836) were purchased from Thermo Fisher Scientific. The antibodies used were as follows: FLAG (F1365; Millipore Sigma-Aldrich), RTN4 (sc-271878; Santa Cruz Biotechnology), RTN3 (A302-860A; Bethyl Laboratories), B12 (16780–1-AP; Proteintech Group), Hsp90 (sc7947; Santa Cruz Biotechnology), dsRNA (J2; Jena Biosciences; 10010200), NSP1 (GTX135612; Genetex), Streptavidin (LS-C203628; LifeSpan BioSciences), HA (11867423001; Roche), FAM134B (21537-1-AP; Proteintech Group), BAP31 (MA3-002; Invitrogen), DNAJB12 (16780-1-AP; Proteintech Group), anti-Mouse IgG Alexa Fluor 488 (A-11029; Invitrogen), anti-Rabbit IgG (A4914; Sigma-Aldrich), anti-Mouse IgG (A4416; Sigma-Aldrich), anti-Rat IgG (A5795; Sigma-Aldrich), and ProLong Diamond Antifade Mountant with DAPI (P36962; Invitrogen).

siRNAs

All Star Negative (Qiagen) was used as a scrambled control siRNA. The following siRNAs were purchased from Millipore Sigma-Aldrich: siRTN3, 5′-UCAGUGUCAUCAGUGUGGUUUCUUADTDT-3′; siRTN4, 5′-GUUCAGAAGUACAGUAAUUDTDT-3′; siFAM134B, 5′-CAAAGATGACAGTGAATTADTDT-3′.

DNA plasmids

2xStrep-NSP3 and NSP4-2xStrep were gifts from Dr. Elizabeth R. Fischer (National Institutes of Health, Hamilton, MT [Hackstadt et al., 2021]). FLAG-NSP2 was a gift from Dr. Lars Plate (Vanderbilt University, Nashville, TN [Davies et al., 2020]). The pcDNA3.1-GFP-Sec61β, pAc-GFP-RTN3C, HA-RTN4B, and GFP-RTN4HD were gifts from Dr. Tom Rapoport (Harvard University, Cambridge, MA [Shibata et al., 2010; Voeltz et al., 2006]). The pcDNA3.1-FLAG-RTN3A was a kind gift from Dr. Ivan Dikic (Goethe University, Frankfurt, Germany [Grumati et al., 2017]). FLAG-HRD1, FLAG-GFP-RTN3C, and FLAG-GFP-RTN4A were described previously (Chen et al., 2021; Chen et al., 2020b).

siRNA and DNA plasmid transfection

For siRNA transfection, Huh7 cells were reverse transfected with 50 nM of the indicated siRNA using Lipofectamine RNAiMAX (Thermo Fisher Scientific). Infections and biochemical assays were performed 48 h after transfection. For DNA plasmid transfection, Huh7 and HEK293T cells were transfected with 1 µg of the indicated DNA plasmids using polyethylenimine (PEI; Polysciences). Infections and biochemical assays were performed 24 h after transfection.

SARS-CoV-2 infection

2×10^5 Huh7 or Vero E6 cells were plated on 12-well plates prior to infection. DMEM containing 10% FBS was replaced with DMEM containing 2% FBS to prevent cell proliferation. Cells were brought into the University of Michigan Biosafety Level-3 laboratory prior to infection. Cells were infected at 2 (or 5) MOI with one of the following SARS-CoV-2 strains: USA-WA1/2020 (NR-52281; Washington); hCoV-19/England/204820464/2020 (alpha; B.1.1.7); hCoV-19/South Africa/KRISP-K005325/2020 (beta; B.1.351); and hCoV-19/USA/PHC658/2021 (delta, B.1.617.2). Infected cells were incubated for 4 h, 12 h, 24 h, or 48 h before virus inactivation. SARS-CoV-2 in infected media was inactivated using bleach. SARS-Cov-2 in infected cells were inactivated by either 4% PFA for 30 min, 1.25% glutaraldehyde for 30 min, 1X Laemmli sample buffer at 95°C for 10 min, or by bleaching. For Fig. 2 F, cells were incubated at 4°C for 1 h prior to virus addition. SARS-CoV-2 WA1 was then added at MOI 5 and the cells were again immediately incubated at 4°C to synchronize infection. The cells were then transferred to 37°C for 4 h as indicated.

Immunoblotting

For immunoblotting, cells were lysed in 100 µl RIPA buffer supplemented with 10 mM NEM and 1 mM PMSF, incubated on ice for 10 min, and centrifuged. The extract was subjected to SDS-PAGE and transferred to either nitrocellulose or PVDF membrane. Membranes were incubated with primary antibodies in TBST with 3% milk or BSA overnight, washed, and incubated with secondary antibodies for 30–60 min prior to exposure using ECL. For immunoblotting samples infected with SARS-CoV-2, after lysis, the resulting lysate was precipitated with 10% TCA. The resulting pellet was resolved in 1× Laemmli buffer and then incubated at 95°C for 10 min before being subjected to SDS-PAGE and immunoblotting as described above. Images were acquired via autoradiography film (NC9556985; Thermo Fisher Scientific), scanned, and quantified using FIJI distribution of ImageJ.

$TCID_{50}$/ml

After 48 h of infection, media from infected Huh7 or Vero E6 cells containing the secreted virus was harvested and cleared of cell debris via centrifugation. Vero E6 cells were plated on a 96-well plate at 2×10^4 with complete DMEM containing 2% FBS. The cleared media from infected Huh7 or Vero E6 cells was then diluted 10-fold into the first column of uninfected Vero E6 containing 96-well plate and then 10-fold serial dilutions of the infected media were added to each subsequent column of wells down to the eighth column. As a control, a column of wells was left uninfected. The 96-well plate was then incubated for 48 h and then scored for the cytopathic effect (CPE). After scoring wells for CPE, the $TCID_{50}$/ml was calculated using the Shi-Hsia Hwa $TCID_{50}$/ml calculator (licensed by Creative Commons Attribution-ShareAlike 4.0 International), which determines the $TCID_{50}$/ml using the Reed-Muench method.

dsRNA immunofluorescent imaging

Huh7 or Vero E6 cells were grown on no.1 glass coverslips, infected with SARS-CoV-2 WA1 for 48 h, and then chemically fixed

with 4% PFA for 30 min. Cells were then permeabilized in PBS with 0.2% Triton X-100 for 5 min and blocked with 5% milk containing 0.05% Tween-20. Primary antibodies were incubated in milk overnight at 4°C. Coverslips were then washed four times in milk and incubated with Alexa Fluor secondary antibodies (Invitrogen) for 30 min at room temperature. Coverslips were again washed and mounted using ProLong Gold with DAPI (Invitrogen). Images were taken using a 40× objective on a Nikon Eclipse TE2000-E inverted epifluorescence microscope at room temperature. Images were acquired using NIS Elements imaging software (Nikon version 4.60). FIJI software was used for image processing and analysis. Briefly, cells displaying the anti-dsRNA signal were counted and divided by the total number of cells in each field indicated by DAPI staining.

RT-qPCR

After PFA fixation, RNA from infected Huh7 cells was extracted using TRIzol Reagent (15596018; Thermo Fisher Scientific) according to the manufacturer's protocol. The concentrations of the extracted RNA were determined using a NanoDrop 2000 spectrophotometer (ND2000CLAPTOP; Thermo Fisher Scientific). RNA conversion to DNA was achieved by using iScript Reverse Transcription Supermix for RT-qPCR (1708841; Bio-Rad) using 0.5 µg of RNA following the manufacturer's protocol. qPCR was subsequently performed using the SsoAdvanced Universal SYBR Green Supermix (1725271; Bio-Rad) on a CFX Connect Real-Time PCR Detection System (Bio-Rad, 1855201) along with Bio-Rad CFX Maestro Software according to the manufacturer's protocol. Briefly, 100 ng of template DNA was mixed with the SYBR Supermix along with 5 µM each forward and reverse primers. qPCR was performed at 95°C for 10 s, 60°C for 40 s, for 50 cycles, followed by melt curve analysis at 65°C for 5 s then 95°C for 5 s. Primers used were: SARS-CoV-2_Orf1a_Forward, 5′-GTGCTCATGGATGGCTCTATTA-3′; SARS-CoV-2_Orf1a_Reverse, 5′-CGTGCCTACAGTACTCAGAATC-3′; GAPDH_Forward, 5′-CCC TTCATTGACCTCAACTACA-3′; GAPDH_Reverse, 5′-ATGACA AGCTTCCCGTTCTC-3′. qPCR of each sample was done using three technical replicates with SARS-CoV-2 Orf1a primers as well as three technical replicates using primers against GAPDH. Average cycle threshold (Ct) values were calculated followed by delta–delta Ct values for each sample as described (Livak and Schmittgen, 2001).

Transmission electron microscopy (TEM)

For TEM, 2 × 10^5 Huh7 cells were plated on 35-mm MatTek glass bottom dishes (MatTek Co., P35G-1.5-10-C). After siRNA transfection, the cells were infected for 12 h or 24 h. Warm 2.5% glutaraldehyde in 0.1 M sodium cacodylate buffer at 37°C was added to the cell media to optimally dilute the fixative. The cells were initially fixed for 30 min at room temperature and then additionally fixed overnight at 4°C. Following the pre-fixation, cells were washed with 0.1 M sodium cacodylate buffer (11654; Electron Microscopy Sciences) to remove residual aldehyde. For lipid fixation, the cells were postfixed with a mixture of ice-cold 1% osmium tetroxide (4% OsO4, 19140; Electron Microscopy Sciences) and 1% potassium ferrocyanide (10% K4FeCN6, 25154-10; Electron Microscopy Sciences) in 0.1 M sodium cacodylate buffer for 15 min on ice. Cells were then washed with 0.1 M sodium cacodylate buffer. To enhance the contrast of cell membrane and subcellular membrane, the cells were treated with 4X diluted uranyl acetate replacement stain (22405; Electron Microscopy Sciences) for 15 min at room temperature and Walton's lead aspirate for 5 min at 60°C. The cells were washed with distilled water and then dehydrated with ascending ethanol series (10, 30, 50, 70, 80, 90, 95, and 100%). The cells were gradually infiltrated with Spurr's resin (14300; Electron Microscopy Sciences) and polymerized for 24 h at 70°C. 70-nm ultrathin sections from polymerized resin blocks were sectioned using an ultramicrotome (Leica EM UC7; Leica Microsystems Inc.), transferred on bare Cu 300 mesh grids, and evaporated with carbon using a high vacuum coater (Leica EM ACE600; Leica Microsystems Inc.). The sections were observed under a Jeol JEM-1400 Plus LaB6 transmission electron microscope (Jeol Inc.) at 60 keV and imaged under a 12-megapixel CMOS TEM camera (Advanced Microscopy Techniques, NanoSprint12). Pseudo-coloring of the ER in red was done using Adobe Photoshop.

Immunoprecipitation

For IP of FLAG-tagged proteins, HEK 293T cells transfected with FLAG-Hrd1, FLAG-RTN3A, or FLAG-GFP-RTN3C were seeded in 15-cm plates. The cells were lysed in 1% DBC in a physiological buffer at 4°C for 10 min and centrifuged at 13,000 × g at 4°C for 10 min. The supernatant was collected and rotated at 4°C for 2 h with M2 FLAG-conjugated beads. The beads were washed three times and the bound material was eluted by 3xFLAG peptide and subjected to SDS-PAGE, followed by immunoblotting using the indicated antibodies. For IP of HA-tagged proteins, HEK 293T cells were transfected with HA-GFP or HA-RTN4B. Cells were lysed as above, and the supernatant was collected and rotated at 4°C overnight with anti-HA magnetic beads. The beads were washed three times in a lysis buffer. The beads were then treated with 1× Laemmli sample buffer and subjected to SDS-PAGE and immunoblotting using the indicated antibodies.

Protein expression and purification for in vitro binding studies

Purification of FLAG-tagged proteins

HEK 293T cells transiently expressing FLAG-GFP, FLAG-RTN3A, or FLAG-GFP-RTN4A were lysed in a buffer containing 150 mM NaCl, 50 mM HEPES, and 1% deoxy Big CHAP with 1 mM PMSF. Samples were pelleted at high speed to remove unbroken cells and debris, and the supernatant was subject to FLAG immunopurification using anti-FLAG affinity gel (Cat#12657; Millipore Sigma) for 2 h at 4°C. The samples were then washed five times with lysis buffer, and FLAG-GFP, FLAG-RTN3A, or FLAG-GFP-RTN4A was eluted using excess 3xFLAG peptide.

Purification of 2xStrep-NSP3 and NSP4-2xStrep

HEK 293T cells transiently expressing 2xStrep-NSP3 or NSP4-2xStrep were lysed in a buffer containing 150 mM NaCl, 50 mM HEPES, and 1% deoxy Big CHAP with 1 mM PMSF. Samples were pelleted at high speed to remove unbroken cells and debris, and the supernatant was subject to strep immunopurification using

MagStrep "type3" XT beads (Cat#126572-4090-002; IBA Lifesciences) overnight at 4°C. The samples were then washed five times with lysis buffer, and 2xStrep-NSP3 and NSP4-2xStrep were eluted using Buffer E (0.1 M Tris-Cl, 150 mM NaCl, 1 mM EDTA, 2.5 mM desthiobiotin).

In vitro binding

250 ng of 2xStrep-NSP3 or NSP4-2xStrep was incubated with either 0.25 ug of FLAG-GFP, FLAG-RTN3A, or FLAG-GFP-RTN4A in a lysis buffer for 30 min at 37°C and immunoprecipitated using MagStrep "type3" XT beads for 15 min at 4°C. Samples were washed five times in a lysis buffer and eluted with sample buffer. Samples were subjected to SDS-PAGE and immunoblotting using the indicated antibodies.

MTS assay

Huh7 cells were plated on 96-well plates at a density of 2×10^4 cells per well and transfected with the indicated siRNAs for either 48 h or 96 h. The cells were treated with the MTS reagent (ab197010; MTS Assay Kit, Abcam) according to the manufacturer's protocol and incubated at 37°C under 5% CO_2 for 1 h. The plate was briefly vortexed and absorbance (OD = 490 nm) was read using a BioTek Synergy H1 Multimode Reader (Agilent). The data were analyzed using BioTek Gen5 software.

XBP1 splicing

Huh7 cells were transfected with either scrambled, RTN3, or RTN4 siRNA. As a positive control, one sample was treated for 2 h with 1 mM DTT to induce XBP1 splicing. In brief, cells were collected and total RNA was extracted using the RNeasy Mini Kit (74104; Qiagen). cDNA was generated from the extracted RNA using the iScript Reverse Transcription kit (1708841; BioRad). XBP1 fragments were then amplified using the following primers: 5′-CGCGGATCCGAATGTGAGGCCAGTGG-3′ and 5′-GGG GCTTGGTATATATGTGG-3′. The amplified fragments were separated on an acrylamide gel, and images were acquired with a UVP BioDoc-It Imaging system.

Confocal imaging

Huh7 cells were grown on number 1 glass coverslips and chemically fixed with 4% PFA for 15 min. Cells were then permeabilized in PBS with 0.2% Triton X-100 for 10 min and blocked with 5% milk containing 0.02% Tween-20. Anti-DNAJB12 and DAPI were incubated in milk overnight at 4°C. Coverslips were then washed four times in milk and incubated with Alexa Fluor secondary (Invitrogen) for 1 h at room temperature. Coverslips were again washed and mounted using ProLong Gold (Invitrogen) and imaged using the Zeiss LSM 780 confocal microscope using a 63× objective at room temperature. Images were acquired using ZEN Microscopy software (Zeiss). FIJI software was used for image processing and analysis.

Quantification and statistical analysis

All data obtained from at least three independent experiments (biological replicates) were combined for statistical analyses. Results were analyzed using Student's two-tailed *t* test. Data are represented as the mean values, and the error bar represents SD, where indicated. The P values are indicated by *P < 0.05, **P < 0.01, and ***P < 0.001. P < 0.05 was considered to be significant.

Online supplemental material

Fig. S1 contains a schematic outlining the time points for key experiments, validation of other siRNAs in Vero E6 cells, graphs from Fig. 1 using logarithmic scaling, and various assays demonstrating the siRNAs do not globally disrupt cell integrity. Fig. S2 contains additional representative images related to Fig. 3, and Fig. S3 shows TEM images from Fig. 3 with the ER pseudocolored showing a lack of change in ER morphology using the indicated siRNAs. Fig. S4 shows the NSP levels via immunoblotting at 12 h.p.i. using the indicated siRNAs. All data are available in the article itself and its supplementary materials.

Acknowledgments

We thank members of the Tsai and Tai laboratories for their helpful suggestions.

B. Tsai is funded by the National Institutes of Health (RO1 AI170514).

Author contributions: J.M. Williams and Y.J. Chen designed and performed experiments for Figs. 1, 2, 3, 4 E, S1, S2, and S4. Y.J. Chen designed and performed experiments for Figs. 4, A, B, C, and D, and Fig. S3. W.J. Cho helped design and perform experiments for Fig. 3 and Fig. S2. J.M. Williams, Y.J. Chen, A.W. Tai, and B. Tsai conceived the project, designed the experiments, and wrote the manuscript.

Disclosures: The authors declare no competing interests exist.

Submitted: 17 March 2022
Revised: 24 August 2022
Accepted: 6 April 2023

References

Al-Mulla, H.M., L. Turrell, N.M. Smith, L. Payne, S. Baliji, R. Züst, V. Thiel, S.C. Baker, S.G. Siddell, and B.W. Neuman. 2014. Competitive fitness in coronaviruses is not correlated with size or number of double-membrane vesicles under reduced-temperature growth conditions. *MBio.* 5:e01107–e01113. https://doi.org/10.1128/mBio.01107-13

Angelini, M.M., M. Akhlaghpour, B.W. Neuman, and M.J. Buchmeier. 2013. Severe acute respiratory syndrome coronavirus nonstructural proteins 3, 4, and 6 induce double-membrane vesicles. *MBio.* 4:4. https://doi.org/10.1128/mBio.00524-13

Chen, Y.J., P. Bagchi, and B. Tsai. 2020a. ER functions are exploited by viruses to support distinct stages of their life cycle. *Biochem. Soc. Trans.* 48: 2173–2184. https://doi.org/10.1042/BST20200395

Chen, Y.J., J.M. Williams, P. Arvan, and B. Tsai. 2020b. Reticulon protects the integrity of the ER membrane during ER escape of large macromolecular protein complexes. *J. Cell Biol.* 219:e201908182. https://doi.org/10.1083/jcb.201908182

Chen, Y.J., J. Knupp, A. Arunagiri, L. Haataja, P. Arvan, and B. Tsai. 2021. PGRMC1 acts as a size-selective cargo receptor to drive ER-phagic clearance of mutant prohormones. *Nat. Commun.* 12:5991. https://doi.org/10.1038/s41467-021-26225-8

Coronaviridae Study Group of the International Committee on Taxonomy of Viruses. 2020. The species Severe acute respiratory syndrome-related coronavirus: classifying 2019-nCoV and naming it SARS-CoV-2. *Nat. Microbiol.* 5:536–544. https://doi.org/10.1038/s41564-020-0695-z

Cortese, M., J.Y. Lee, B. Cerikan, C.J. Neufeldt, V.M.J. Oorschot, S. Köhrer, J. Hennies, N.L. Schieber, P. Ronchi, G. Mizzon, et al. 2020. Integrative

imaging reveals SARS-CoV-2-induced reshaping of subcellular morphologies. *Cell Host Microbe*. 28:853–866.e5. https://doi.org/10.1016/j.chom.2020.11.003

Cunningham, C.N., J.M. Williams, J. Knupp, A. Arunagiri, P. Arvan, and B. Tsai. 2019. Cells deploy a two-pronged strategy to rectify misfolded proinsulin aggregates. *Mol. Cell*. 75:442–456.e4. https://doi.org/10.1016/j.molcel.2019.05.011

Davies, J.P., K.M. Almasy, E.F. McDonald, and L. Plate. 2020. Comparative multiplexed interactomics of SARS-CoV-2 and homologous coronavirus nonstructural proteins identifies unique and shared host-cell dependencies. *ACS Infect. Dis.* 6:3174–3189. https://doi.org/10.1021/acsinfecdis.0c00500

Di Scala, F., L. Dupuis, C. Gaiddon, M. De Tapia, N. Jokic, J.L. Gonzalez de Aguilar, J.S. Raul, B. Ludes, and J.P. Loeffler. 2005. Tissue specificity and regulation of the N-terminal diversity of reticulon 3. *Biochem. J.* 385:125–134. https://doi.org/10.1042/BJ20040458

Diaz, A., and P. Ahlquist. 2012. Role of host reticulon proteins in rearranging membranes for positive-strand RNA virus replication. *Curr. Opin. Microbiol.* 15:519–524. https://doi.org/10.1016/j.mib.2012.04.007

Dong, E., H. Du, and L. Gardner. 2020. An interactive web-based dashboard to track COVID-19 in real time. *Lancet Infect. Dis.* 20:533–534. https://doi.org/10.1016/S1473-3099(20)30120-1

Froshauer, S., J. Kartenbeck, and A. Helenius. 1988. Alphavirus RNA replicase is located on the cytoplasmic surface of endosomes and lysosomes. *J. Cell Biol.* 107:2075–2086. https://doi.org/10.1083/jcb.107.6.2075

Geisler, J.G., L.J. Stubbs, W.W. Wasserman, and M.L. Mucenski. 1998. Molecular cloning of a novel mouse gene with predominant muscle and neural expression. *Mamm. Genome*. 9:274–282. https://doi.org/10.1007/s003359900748

GrandPré, T., F. Nakamura, T. Vartanian, and S.M. Strittmatter. 2000. Identification of the Nogo inhibitor of axon regeneration as a Reticulon protein. *Nature*. 403:439–444. https://doi.org/10.1038/35000226

Grumati, P., G. Morozzi, S. Hölper, M. Mari, M.I. Harwardt, R. Yan, S. Müller, F. Reggiori, M. Heilemann, and I. Dikic. 2017. Full length RTN3 regulates turnover of tubular endoplasmic reticulum via selective autophagy. *Elife*. 6:e25555. https://doi.org/10.7554/eLife.25555

Hackstadt, T., A.I. Chiramel, F.H. Hoyt, B.N. Williamson, C.A. Dooley, P.A. Beare, E. de Wit, S.M. Best, and E.R. Fischer. 2021. Disruption of the golgi apparatus and contribution of the endoplasmic reticulum to the SARS-CoV-2 replication complex. *Viruses*. 13:1798. https://doi.org/10.3390/v13091798

Hagemeijer, M.C., I. Monastyrska, J. Griffith, P. van der Sluijs, J. Voortman, P.M. van Bergen en Henegouwen, A.M. Vonk, P.J. Rottier, F. Reggiori, and C.A. de Haan. 2014. Membrane rearrangements mediated by coronavirus nonstructural proteins 3 and 4. *Virology*. 458-459:125–135. https://doi.org/10.1016/j.virol.2014.04.027

Hoffmann, M., H. Kleine-Weber, S. Schroeder, N. Krüger, T. Herrler, S. Erichsen, T.S. Schiergens, G. Herrler, N.H. Wu, A. Nitsche, et al. 2020. SARS-CoV-2 cell entry depends on ACE2 and TMPRSS2 and is blocked by a clinically proven protease inhibitor. *Cell*. 181:271–280.e8. https://doi.org/10.1016/j.cell.2020.02.052

Ji, M., M. Li, L. Sun, H. Zhao, Y. Li, L. Zhou, Z. Yang, X. Zhao, W. Qu, H. Xue, et al. 2022. VMP1 and TMEM41B are essential for DMV formation during β-coronavirus infection. *J. Cell Biol.* 221:e202112081. https://doi.org/10.1083/jcb.202112081

Khaminets, A., T. Heinrich, M. Mari, P. Grumati, A.K. Huebner, M. Akutsu, L. Liebmann, A. Stolz, S. Nietzsche, N. Koch, et al. 2015. Regulation of endoplasmic reticulum turnover by selective autophagy. *Nature*. 522:354–358. https://doi.org/10.1038/nature14498

Kim, D., J.Y. Lee, J.S. Yang, J.W. Kim, V.N. Kim, and H. Chang. 2020. The architecture of SARS-CoV-2 transcriptome. *Cell*. 181:914–921.e10. https://doi.org/10.1016/j.cell.2020.04.011

Klaus, J.P., P. Eisenhauer, J. Russo, A.B. Mason, D. Do, B. King, D. Taatjes, C. Cornillez-Ty, J.E. Boyson, M. Thali, et al. 2013. The intracellular cargo receptor ERGIC-53 is required for the production of infectious arenavirus, coronavirus, and filovirus particles. *Cell Host Microbe*. 14:522–534. https://doi.org/10.1016/j.chom.2013.10.010

Klein, S., M. Cortese, S.L. Winter, M. Wachsmuth-Melm, C.J. Neufeldt, B. Cerikan, M.L. Stanifer, S. Boulant, R. Bartenschlager, and P. Chlanda. 2020. SARS-CoV-2 structure and replication characterized by in situ cryo-electron tomography. *Nat. Commun.* 11:5885. https://doi.org/10.1038/s41467-020-19619-7

Klumperman, J., J.K. Locker, A. Meijer, M.C. Horzinek, H.J. Geuze, and P.J. Rottier. 1994. Coronavirus M proteins accumulate in the Golgi complex beyond the site of virion budding. *J. Virol.* 68:6523–6534. https://doi.org/10.1128/jvi.68.10.6523-6534.1994

Knoops, K., M. Kikkert, S.H. Worm, J.C. Zevenhoven-Dobbe, Y. van der Meer, A.J. Koster, A.M. Mommaas, and E.J. Snijder. 2008. SARS-coronavirus replication is supported by a reticulovesicular network of modified endoplasmic reticulum. *PLoS Biol.* 6:e226. https://doi.org/10.1371/journal.pbio.0060226

Livak, K.J., and T.D. Schmittgen. 2001. Analysis of relative gene expression data using real-time quantitative PCR and the 2(-Delta Delta C(T)) Method. *Methods*. 25:402–408. https://doi.org/10.1006/meth.2001.1262

Lu, R., X. Zhao, J. Li, P. Niu, B. Yang, H. Wu, W. Wang, H. Song, B. Huang, N. Zhu, et al. 2020. Genomic characterisation and epidemiology of 2019 novel coronavirus: Implications for virus origins and receptor binding. *Lancet*. 395:565–574. https://doi.org/10.1016/S0140-6736(20)30251-8

McBride, C.E., J. Li, and C.E. Machamer. 2007. The cytoplasmic tail of the severe acute respiratory syndrome coronavirus spike protein contains a novel endoplasmic reticulum retrieval signal that binds COPI and promotes interaction with membrane protein. *J. Virol.* 81:2418–2428. https://doi.org/10.1128/JVI.02146-06

Miller, S., and J. Krijnse-Locker. 2008. Modification of intracellular membrane structures for virus replication. *Nat. Rev. Microbiol.* 6:363–374. https://doi.org/10.1038/nrmicro1890

Mirabelli, C., J.W. Wotring, C.J. Zhang, S.M. McCarty, R. Fursmidt, C.D. Pretto, Y. Qiao, Y. Zhang, T. Frum, N.S. Kadambi, et al. 2021. Morphological cell profiling of SARS-CoV-2 infection identifies drug repurposing candidates for COVID-19. *Proc. Natl. Acad. Sci. USA*. 118:e2105815118. https://doi.org/10.1073/pnas.2105815118

Moreira, E.F., C.J. Jaworski, and I.R. Rodriguez. 1999. Cloning of a novel member of the reticulon gene family (RTN3): Gene structure and chromosomal localization to 11q13. *Genomics*. 58:73–81. https://doi.org/10.1006/geno.1999.5807

Oertle, T., M. Klinger, C.A. Stuermer, and M.E. Schwab. 2003. A reticular rhapsody: Phylogenic evolution and nomenclature of the RTN/Nogo gene family. *FASEB J.* 17:1238–1247. https://doi.org/10.1096/fj.02-1166hyp

Ou, X., Y. Liu, X. Lei, P. Li, D. Mi, L. Ren, L. Guo, R. Guo, T. Chen, J. Hu, et al. 2020. Characterization of spike glycoprotein of SARS-CoV-2 on virus entry and its immune cross-reactivity with SARS-CoV. *Nat. Commun.* 11:1620. https://doi.org/10.1038/s41467-020-15562-9

Oudshoorn, D., K. Rijs, R.W.A.L. Limpens, K. Groen, A.J. Koster, E.J. Snijder, M. Kikkert, and M. Bárcena. 2017. Expression and cleavage of Middle East respiratory syndrome coronavirus nsp3-4 polyprotein induce the formation of double-membrane vesicles that mimic those associated with coronaviral RNA replication. *MBio*. 8:e01658-17. https://doi.org/10.1128/mBio.01658-17

Paul, D., S. Hoppe, G. Saher, J. Krijnse-Locker, and R. Bartenschlager. 2013. Morphological and biochemical characterization of the membranous hepatitis C virus replication compartment. *J. Virol.* 87:10612–10627. https://doi.org/10.1128/JVI.01370-13

Pohl, M.O., L. Martin-Sancho, R. Ratnayake, K.M. White, L. Riva, Q.Y. Chen, G. Lieber, I. Busnadiego, X. Yin, S. Lin, et al. 2022. Sec61 inhibitor apratoxin S4 potently inhibits SARS-CoV-2 and exhibits broad-spectrum antiviral activity. *ACS Infect. Dis.* 8:1265–1279. https://doi.org/10.1021/acsinfecdis.2c00008

Ricciardi, S., A.M. Guarino, L. Giaquinto, E.V. Polishchuk, M. Santoro, G. Di Tullio, C. Wilson, F. Panariello, V.C. Soares, S.S.G. Dias, et al. 2022. The role of NSP6 in the biogenesis of the SARS-CoV-2 replication organelle. *Nature*. 606:761–768. https://doi.org/10.1038/s41586-022-04835-6

Sawicki, S.G., and D.L. Sawicki. 1995. Coronaviruses use discontinuous extension for synthesis of subgenome-length negative strands. *Adv. Exp. Med. Biol.* 380:499–506. https://doi.org/10.1007/978-1-4615-1899-0_79

Sawicki, S.G., D.L. Sawicki, and S.G. Siddell. 2007. A contemporary view of coronavirus transcription. *J. Virol.* 81:20–29. https://doi.org/10.1128/JVI.01358-06

Schulte, H.M., and D.L. Healy. 1987. Corticotropin releasing hormone- and adreno-corticotropin-like immunoreactivity in human placenta, peripheral and uterine vein plasma. *Horm. Metab. Res. Suppl.* 16:44–46.

Shang, C., Z. Liu, Y. Zhu, J. Lu, C. Ge, C. Zhang, N. Li, N. Jin, Y. Li, M. Tian, and X. Li. 2022. SARS-CoV-2 causes mitochondrial dysfunction and mitophagy impairment. *Front. Microbiol.* 12:780768. https://doi.org/10.3389/fmicb.2021.780768

Shibata, Y., T. Shemesh, W.A. Prinz, A.F. Palazzo, M.M. Kozlov, and T.A. Rapoport. 2010. Mechanisms determining the morphology of the peripheral ER. *Cell*. 143:774–788. https://doi.org/10.1016/j.cell.2010.11.007

Singh, K.K., G. Chaubey, J.Y. Chen, and P. Suravajhala. 2020. Decoding SARS-CoV-2 hijacking of host mitochondria in COVID-19 pathogenesis. *Am. J. Physiol. Cell Physiol.* 319:C258–C267. https://doi.org/10.1152/ajpcell.00224.2020

Snijder, E.J., R.W.A.L. Limpens, A.H. de Wilde, A.W.M. de Jong, J.C. Zevenhoven-Dobbe, H.J. Maier, F.F.G.A. Faas, A.J. Koster, and M. Bárcena. 2020. A unifying structural and functional model of the coronavirus replication organelle: Tracking down RNA synthesis. *PLoS Biol.* 18: e3000715. https://doi.org/10.1371/journal.pbio.3000715

Speckhart, K., J.M. Williams, and B. Tsai. 2021. How DNA and RNA viruses exploit host chaperones to promote infection. *Viruses*. 13:958. https://doi.org/10.3390/v13060958

Stertz, S., M. Reichelt, M. Spiegel, T. Kuri, L. Martínez-Sobrido, A. García-Sastre, F. Weber, and G. Kochs. 2007. The intracellular sites of early replication and budding of SARS-coronavirus. *Virology*. 361:304–315. https://doi.org/10.1016/j.virol.2006.11.027

Ulasli, M., M.H. Verheije, C.A. de Haan, and F. Reggiori. 2010. Qualitative and quantitative ultrastructural analysis of the membrane rearrangements induced by coronavirus. *Cell. Microbiol.* 12:844–861. https://doi.org/10.1111/j.1462-5822.2010.01437.x

van de Velde, H.J., A.J. Roebroek, N.H. Senden, F.C. Ramaekers, and W.J. Van de Ven. 1994. NSP-encoded reticulons, neuroendocrine proteins of a novel gene family associated with membranes of the endoplasmic reticulum. *J. Cell Sci.* 107:2403–2416. https://doi.org/10.1242/jcs.107.9.2403

Voeltz, G.K., W.A. Prinz, Y. Shibata, J.M. Rist, and T.A. Rapoport. 2006. A class of membrane proteins shaping the tubular endoplasmic reticulum. *Cell*. 124:573–586. https://doi.org/10.1016/j.cell.2005.11.047

V'kovski, P., M. Gerber, J. Kelly, S. Pfaender, N. Ebert, S. Braga Lagache, C. Simillion, J. Portmann, H. Stalder, V. Gaschen, et al. 2019. Determination of host proteins composing the microenvironment of coronavirus replicase complexes by proximity-labeling. *Elife*. 8:e42037. https://doi.org/10.7554/eLife.42037

V'kovski, P., A. Kratzel, S. Steiner, H. Stalder, and V. Thiel. 2021. Coronavirus biology and replication: Implications for SARS-CoV-2. *Nat. Rev. Microbiol.* 19:155–170. https://doi.org/10.1038/s41579-020-00468-6

Walls, A.C., Y.J. Park, M.A. Tortorici, A. Wall, A.T. McGuire, and D. Veesler. 2020. Structure, function, and antigenicity of the SARS-CoV-2 spike glycoprotein. *Cell*. 183:1735. https://doi.org/10.1016/j.cell.2020.11.032

Wolff, G., R.W.A.L. Limpens, J.C. Zevenhoven-Dobbe, U. Laugks, S. Zheng, A.W.M. de Jong, R.I. Koning, D.A. Agard, K. Grünewald, A.J. Koster, et al. 2020a. A molecular pore spans the double membrane of the coronavirus replication organelle. *Science*. 369:1395–1398. https://doi.org/10.1126/science.abd3629

Wolff, G., C.E. Melia, E.J. Snijder, and M. Bárcena. 2020b. Double-membrane vesicles as platforms for viral replication. *Trends Microbiol.* 28:1022–1033. https://doi.org/10.1016/j.tim.2020.05.009

Wu, M.J., P.Y. Ke, J.T. Hsu, C.T. Yeh, and J.T. Horng. 2014. Reticulon 3 interacts with NS4B of the hepatitis C virus and negatively regulates viral replication by disrupting NS4B self-interaction. *Cell. Microbiol.* 16: 1603–1618. https://doi.org/10.1111/cmi.12318

Yang, Y.S., and S.M. Strittmatter. 2007. The reticulons: A family of proteins with diverse functions. *Genome Biol.* 8:234. https://doi.org/10.1186/gb-2007-8-12-234

Yoshida, H., T. Matsui, A. Yamamoto, T. Okada, and K. Mori. 2001. XBP1 mRNA is induced by ATF6 and spliced by IRE1 in response to ER stress to produce a highly active transcription factor. *Cell*. 107:881–891. https://doi.org/10.1016/S0092-8674(01)00611-0

Zhou, P., X.L. Yang, X.G. Wang, B. Hu, L. Zhang, W. Zhang, H.R. Si, Y. Zhu, B. Li, C.L. Huang, et al. 2020. A pneumonia outbreak associated with a new coronavirus of probable bat origin. *Nature*. 579:270–273. https://doi.org/10.1038/s41586-020-2012-7

Zhu, N., D. Zhang, W. Wang, X. Li, B. Yang, J. Song, X. Zhao, B. Huang, W. Shi, R. Lu, et al. 2020. A novel coronavirus from patients with pneumonia in China, 2019. *N. Engl. J. Med.* 382:727–733. https://doi.org/10.1056/NEJMoa2001017

Zurek, N., L. Sparks, and G. Voeltz. 2011. Reticulon short hairpin transmembrane domains are used to shape ER tubules. *Traffic*. 12:28–41. https://doi.org/10.1111/j.1600-0854.2010.01134.x

JCB

Supplemental material

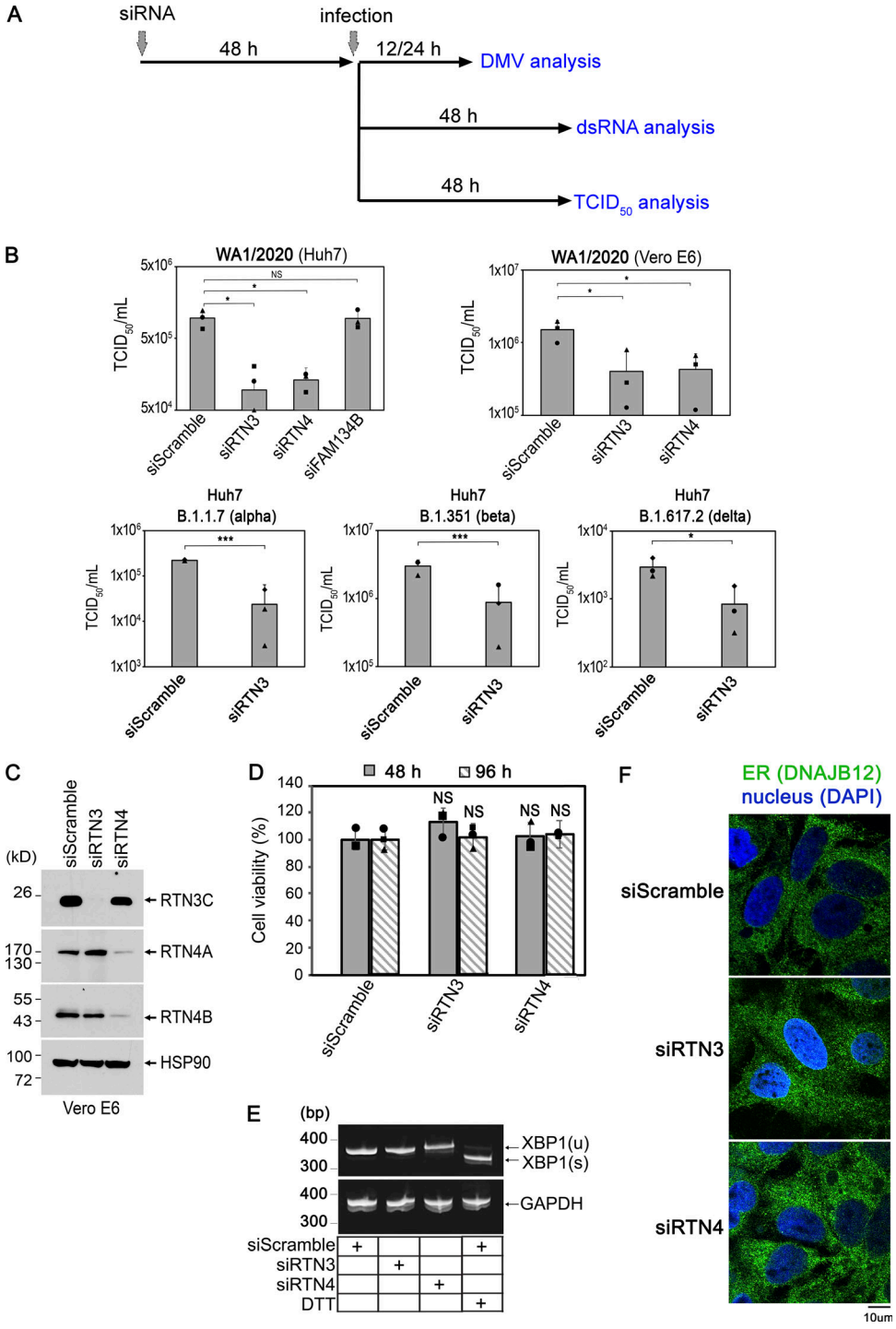

Figure S1. **(Related to Fig. 1). Depletion of RTN3 or RTN4 does not compromise overall cellular integrity. (A)** A working scheme outlining key experiments performed in this manuscript. Briefly, Huh7 or Vero E6 cells were transfected with the indicated siRNAs for 48 h followed by infection for the indicated times before the specific investigation (e.g., DMV, dsRNA, or $TCID_{50}$/ml analysis) was performed. **(B)** Graphs from Fig. 1, B–D with the y-axis in log-scale. **(C)** siRNA KD of RTN3 or RTN4 in Vero E6 cells. Cell extracts derived from Vero E6 cells transfected with the indicated siRNAs were subjected to SDS-PAGE and immunoblotting with the indicated antibodies. **(D)** Huh7 cells were transfected with the indicated siRNAs for 48 or 96 h then subjected to the MTS assay to measure cell viability. Graph represents the percent absorbance relative to control cells for each time point. Data are represented as the mean values and error bars represent means ± SD from three biological replicates. **(E)** Huh7 cells were transfected with the indicated siRNAs for 48 h and treated with or without DTT for 2 h. The splicing of Xbp1 was analyzed by PCR. S indicates spliced XBP1 (ER stress), while U indicates unspliced XBP1 (no ER stress). Primers for GAPDH were analyzed by PCR and serves as the loading control. **(F)** Huh7 cells treated with the indicated siRNAs for 48 h were fixed, permeabilized, stained with anti-DNAJB12 (ER marker) and DAPI, and analyzed by confocal microscopy. NS, not significant where only $P < 0.05$ was considered to be significant. Source data are available for this figure: SourceData FS1.

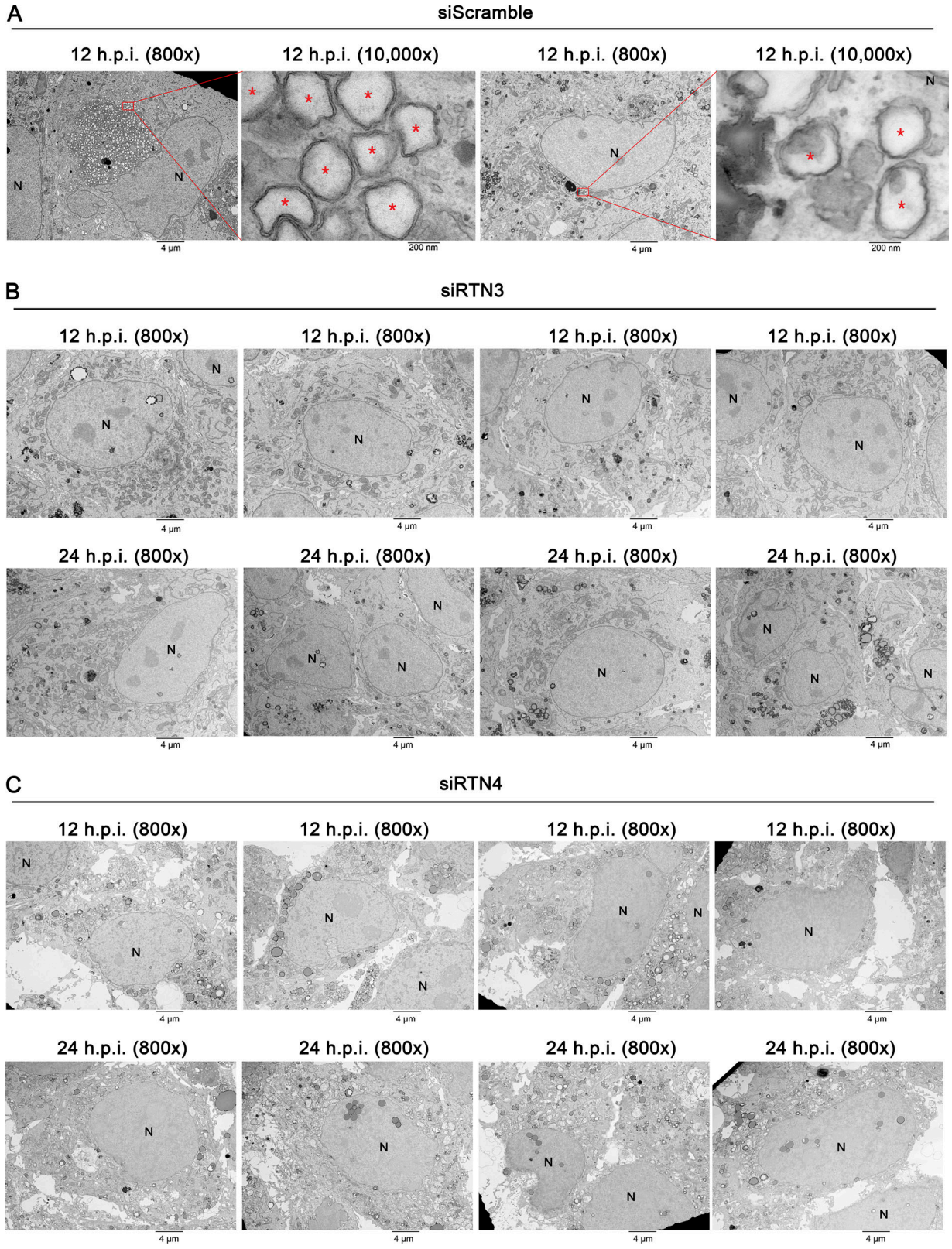

Figure S2. **(Related to Fig. 3). RTN3 and RTN4 are necessary for DMV formation. (A–C)** Additional representative images corresponding to those in Fig. 3. Huh7 cells were treated with the indicated siRNAs and infected with SARS-CoV-2 WA1 at 2 MOI. Scale bars, 4 µm, 200 nm where indicated. **(A)** While patches of peri-nuclear DMVs are evident in control cells (shown at 800× and magnified to 10,000×, where red dots indicate a viral DMV), the DMVs are absent in RTN3 KD (B) and RTN4 KD (C) cells.

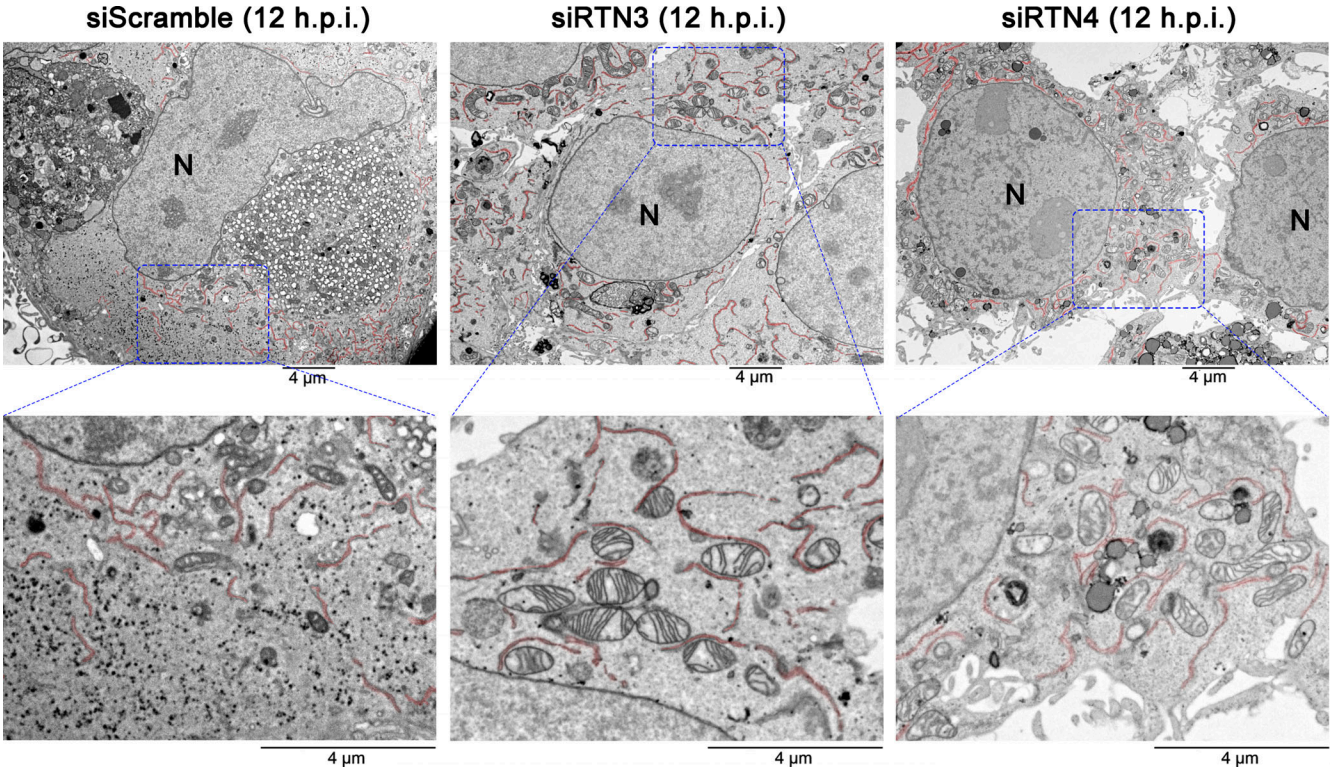

Figure S3. **(Related to Fig. 3). ER morphology in control and RTN-depleted cells.** Representative images from Fig. 3 with the ER highlighted in pink. The images show that the global ER morphology was largely unperturbed under the conditions of RTN depletion when compared to control cells. Huh7 cells were transfected with the indicated siRNAs and infected with SARS-CoV-2 WA1 for 12 h at 2 MOI. Cells were fixed with glutaraldehyde and processed for TEM analysis. The ER was highlighted in pink by using Photoshop. N denotes the nucleus. The top images represent 800× magnification, while the bottom images are zoomed-in sections from the blue boxes in the corresponding images above. Scale bars, 4 µm.

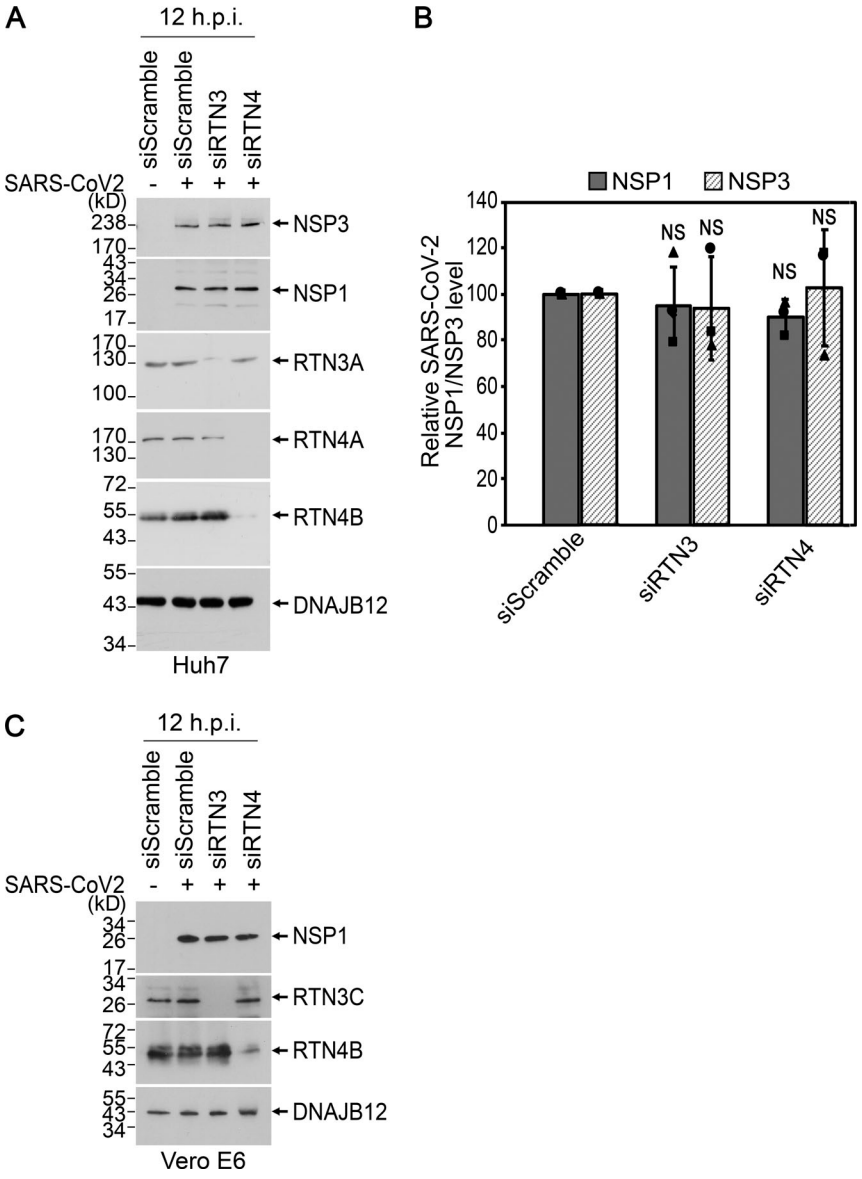

Figure S4. **(Related to Fig. 3). Level of NSP1 and NSP3 in control and RTN-depleted cells. (A)** Huh7 cells were transfected with the indicated siRNAs and then infected (where indicated) with SARS-CoV-2 WA1 at 5 MOI for 12 h and then lysed. The resulting cell extracts were subjected to SDS-PAGE and immunoblotting with the indicated antibodies. **(B)** Quantification of the NSP1 and NSP3 levels relative to control cells in A. Error bars represent means ± SD from three biological replicates. NS, not significant where only $P < 0.05$ was considered to be significant. **(C)** Vero E6 cells were transfected with the indicated siRNAs and then infected (where indicated) with SARS-CoV-2 WA1 at 5 MOI for 12 h and then lysed. The resulting cell extracts were subjected to SDS-PAGE and immunoblotting with the indicated antibodies. Source data are available for this figure: SourceData FS4.